

See discussions, stats, and author profiles for this publication at: <https://www.researchgate.net/publication/262885593>

Photoemission Spectra and Density Functional Theory Calculations of 3d Transition Metal–Aqua Complexes (Ti–Cu) in Aqueous Solution

ARTICLE *in* THE JOURNAL OF PHYSICAL CHEMISTRY B · JUNE 2014

Impact Factor: 3.3 · DOI: 10.1021/jp5012389 · Source: PubMed

CITATIONS

5

READS

71

5 AUTHORS, INCLUDING:



Diana Yepes

Universidad Andrés Bello

10 PUBLICATIONS 71 CITATIONS

SEE PROFILE



Pablo Jaque

Universidad Andrés Bello

51 PUBLICATIONS 996 CITATIONS

SEE PROFILE

Photoemission Spectra and Density Functional Theory Calculations of 3d Transition Metal–Aqua Complexes (Ti–Cu) in Aqueous Solution

Diana Yepes,^{†,⊥} Robert Seidel,^{‡,⊥} Bernd Winter,^{*,§} Jochen Blumberger,^{*,||} and Pablo Jaque^{*,†}

[†]Departamento de Ciencias Químicas, Facultad de Ciencias Exactas, Universidad Andres Bello, Avenida Republica 275, Santiago 8370146, Chile

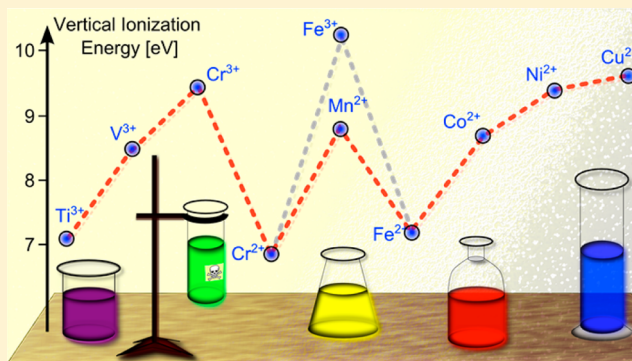
[‡]Department of Chemistry, University of Southern California, 920 Bloom Walk, Los Angeles, California 90089, United States

[§]Joint Laboratory for Ultrafast Dynamics in Solutions and at Interfaces (JULiq), Helmholtz–Zentrum Berlin für Materialien und Energie, and BESSY II, Albert–Einstein–Strasse 15, D-12489 Berlin, Germany

^{||}Department of Physics and Astronomy, University College London, London WC1E6BT, United Kingdom

S Supporting Information

ABSTRACT: Photoelectron spectroscopy measurements and density functional calculations are combined to determine the lowest electron binding energies of first-row transition-metal aqua ions, titanium through copper, with 3d¹ through 3d⁹ electronic configurations, in their most common oxidation states. Vertical ionization energies are found to oscillate considerably between 6.76 and 9.65 eV for the dications and between 7.05 and 10.28 eV for the respective trivalent cations. The metal cations are modeled as [M(H₂O)_n]^{q+} clusters ($q = 2, 3$, and 4; $n = 6$ and 18) surrounded by continuum solvent. The performance of 10 exchange–correlation functionals, two GGAs, three MGGAs, two HGGAs and three HMGGAs, combined with the MDF10(ECP)/6-31+G(d,p) basis set is assessed for 11 M–O bond distances, 10 vertical ionization energies, 6 adiabatic ionization energies, and the associated reorganization free energies. We find that for divalent cations the HGGa and HMGGa functionals in combination with the 18 water model show the best agreement with experimental vertical ionization energies and geometries; for trivalent ions, the MGGa functionals perform best. The corresponding reorganization free energies (λ_o) of the oxidized ions are significantly underestimated with all DFT functionals and cluster models. This indicates that the structural reorganization of the solvation shell upon ionization is not adequately accounted for by the simple solvation models used, emphasizing the importance of extended sampling of thermally accessible solvation structures for an accurate computation of this quantity. The photoelectron spectroscopy measurements reported herein provide a comprehensive set of transition-metal redox energetic quantities for future electronic structure benchmarks.



1. INTRODUCTION

Knowledge of the geometry of transition-metal (TM) cations in aqueous solution and of the underlying electronic–structure interactions with the water solvent are essential for understanding their chemistry, for instance, in catalysis, electrochemistry, photochemistry, and biochemistry.¹ TM ions are stable in a variety of oxidation states and act as redox-active centers that are able to form complexes with charged and neutral molecules, which are essential for biological processes, such as the regulation of metabolic processes, signaling functions in cells, enzymatic catalysis, and electron transport.¹ A diverse array of structural motifs of hydrated TM ions has been experimentally obtained by X-ray diffraction (XD)² in the solid state and by Raman and infrared (IR) spectroscopies,^{3–6} large-angle X-ray scattering (LAXS), X-ray emission spectroscopies,^{7–9} and neutron scattering (NS)^{10–12} in aqueous

solution. Some of these methods are sensitive to the local structure and the chemical surroundings, providing fairly accurate information on the first hydration shell composition and structure.^{13–15}

From a chemical reactivity viewpoint, TM cations play an important role in chemical reactions involving electron transfer, both with and without the breaking and/or forming of chemical bonds. A key thermodynamic descriptor for the extent of gaining or losing electron charge by a chemical species is the redox potential, which can be measured, for example, by cyclic voltammetry. Taking the half-cell reaction in the oxidation direction

Received: February 4, 2014

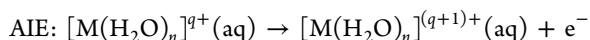
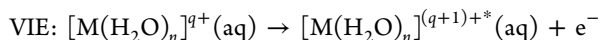
Revised: May 16, 2014

Published: May 16, 2014

Table 1. Experimental Results for All Transition-Metal Salt Solutions Used in This Study^a

TM ion	salt used	conc. (m)	pH	majority species	VIE (eV)	fwhm (eV)
d ¹ Ti ³⁺	TiCl ₃ ·HCl	0.8	−0.37	[TiCl(H ₂ O) ₅] ²⁺	7.05 ± 0.03	1.30 ± 0.06
d ² V ³⁺	VCl ₃	0.465	1.73	[V(H ₂ O) ₆] ³⁺	8.41 ± 0.06	1.13 ± 0.10
d ³ Cr ³⁺	CrCl ₃ ·6H ₂ O	1.0	2.80	[CrCl ₂ (H ₂ O) ₄] ⁺	8.75 ± 0.01	0.90 ± 0.02
	Cr(NO ₃) ₃ ·9H ₂ O	0.25	2.19	[Cr(H ₂ O) ₆] ³⁺	9.44 ± 0.02	1.05 ± 0.02
		1.0	1.31		9.54 ± 0.01	1.17 ± 0.02
	Cr(ClO ₄) ₃ ·6H ₂ O	0.5	1.70		9.46 ± 0.01	0.94 ± 0.01
d ⁴ Cr ²⁺	CrCl ₂	0.9	1.49	[Cr(H ₂ O) ₆] ²⁺	6.76 ± 0.09	1.05 ± 0.13
d ⁵ Mn ²⁺	MnCl ₂ ·4H ₂ O	0.25	5.28	[Mn(H ₂ O) ₆] ²⁺	8.77 ± 0.03	1.13 ± 0.07
	Mn(NO ₃) ₂ ·4H ₂ O	0.25	3.89		8.87 ± 0.04	1.35 ± 0.09
d ⁵ Fe ³⁺	FeCl ₃ ·6H ₂ O	0.25	1.00	[Fe(H ₂ O) ₅ OH] ²⁺	9.75 ± 0.45	1.48 ± 0.51
		1.0	0.42	[FeCl ₂ (H ₂ O) ₄] ⁺	9.38 ± 0.02	0.99 ± 0.02
	Fe(NO ₃) ₃ ·9H ₂ O	0.25	1.10	[Fe(H ₂ O) ₆] ³⁺	10.28 ± 0.04	0.75 ± 0.17
		1.5	0.15	[Fe(H ₂ O) ₅ OH] ²⁺	10.10 ± 0.04	0.76 ± 0.08
d ⁶ Fe ²⁺	FeCl ₂ ·4H ₂ O	0.25	2.84	[Fe(H ₂ O) ₆] ²⁺	7.13 ± 0.02	1.03 ± 0.05
d ⁷ Co ²⁺	CoCl ₂ ·6H ₂ O	0.25	3.81	[Co(H ₂ O) ₆] ²⁺	8.67 ± 0.12	1.04 ± 0.13
		1.75	2.68	[CoCl(H ₂ O) ₅] ⁺	8.65 ± 0.04	1.04 ± 0.04
	Co(NO ₃) ₂ ·6H ₂ O	0.25	5.02	[Co(H ₂ O) ₆] ²⁺	8.72 ± 0.10	1.15 ± 0.11
		0.5	4.88		8.71 ± 0.05	1.03 ± 0.07
d ⁸ Ni ²⁺	NiCl ₂ ·6H ₂ O	0.25	6.71	[Ni(H ₂ O) ₆] ²⁺	9.42 ± 0.01	0.96 ± 0.01
		0.5	6.14		9.41 ± 0.01	0.98 ± 0.05
		1.0	5.88		9.46 ± 0.01	1.06 ± 0.02
		2.0	5.24		9.46 ± 0.01	1.05 ± 0.01
	Ni(NO ₃) ₂ ·6H ₂ O	0.25	4.23		9.43 ± 0.01	0.91 ± 0.03
		0.5	3.98		9.48 ± 0.01	0.98 ± 0.03
d ⁹ Cu ²⁺	NiI ₂	0.2	3.61		9.44 ± 0.09	0.95 ± 0.18
		0.4	3.35		9.48 ± 0.01	0.97 ± 0.02
	CuCl ₂ ·2H ₂ O	0.25	3.34	[Cu(H ₂ O) ₆] ²⁺	9.63 ± 0.03	0.93 ± 0.12
		1.75	1.47	[CuCl ₂ (H ₂ O) ₄]	9.17 ± 0.02	1.08 ± 0.05
	Cu(NO ₃) ₂ ·3H ₂ O	0.25	3.45	[Cu(H ₂ O) ₆] ²⁺	9.61 ± 0.07	0.90 ± 0.17
		2.0	1.61		9.71 ± 0.07	1.08 ± 0.08

^aError margins for the VIE and the full-width at half maximum of the respective Gaussian peak fit reflect the statistical error.



$$(n = 6, 18) \quad (4)$$

2. METHODS AND MATERIALS

2.1. Experimental Section. PE spectroscopy measurements of TM aqua complexes were performed at the U41-PGM undulator beamline of the synchrotron radiation facility BESSY II, Berlin. Spectra were collected from a 24 μm vacuum liquid jet traveling at a velocity of 40 ms^{−1} with a temperature of 10 °C. Details of the technique and experimental setup have been described previously.^{18,21,30,31} Briefly, photoelectrons were detected normal to both the synchrotron light polarization vector and the flow of the liquid jet. Photoelectrons pass through a 150 μm diameter orifice, which separates the main interaction chamber (10^{−4} mbar pressure under operation conditions) from the differentially pumped detector chamber (10^{−8} mbar), housing a hemispherical electron-energy analyzer. The small distance of 0.5 mm between the liquid jet and the orifice assures that detected electrons have not suffered from inelastic scattering with water gas-phase molecules near the jet surface.^{18,21} All valence PE spectra reported here were measured with the lowest photon energies (180 to 200 eV) available at the U41 beamline photon energy. In this energy range, resolution of the beamline was better than 50 meV. The

resolution of the hemispherical energy analyzer was constant with kinetic energy, approximately 100 meV at 10 eV pass energy. The small focal size, 23 × 12 μm², of the incident photon beam matches the diameter of the liquid jet and leads to an almost negligible PE signal from gas-phase water, less than 5% with respect to the total signal.

In order to disentangle contributions from TM ions, which usually overlap with the valence PE peaks of water, reference measurements were performed from solutions containing the same amount of counterions as the respective TM salt solutions. Subtraction of the reference spectrum from the TM–PE spectrum yields, to a good approximation, the sole metal ion electron contribution. This subtraction method can be applied only for PE spectra with a sufficiently good signal-to-noise ratio, and it typically requires salt concentrations of at least 200 mM. For these rather high concentrations, formation of the neat aqua complex may still be dominant, although a considerable fraction of complexes, containing counteranions in the first hydration shell, is likely to form. These latter complexes in water have a different electronic structure (and different VIE), and, except for Ti³⁺(aq), are not considered in the present theoretical calculations. Because we cannot use a lower concentration than the ones reported here, in order to minimize 1-shell water substitution by anions in the current PE spectroscopy experiment we instead compare solutions for different counterions. This provides a reasonably good estimate on speciation (and can be compared with results based on reported dissociation constants); here, we are especially

interested in the cases where the counterion is unlikely to be accommodated within the first coordination sphere, for instance, in the case of large nitrate as compared to small chloride.

All aqueous solutions were prepared using highly demineralized water ($>17 \text{ MOhm cm}^{-1}$). Measurements of the pH, performed with a Greisinger pH meter, reveal variable degrees of acidity, ranging from pH -0.37 for 0.8 m TiCl_3 to pH 6.71 for 0.25 m NiCl_2 in water. Values for all solutions are summarized in Table 1, where we also present the results from the PE measurements (see results in Section 4). In the Supporting Information, we present a brief description of the preparation of the individual TM aqueous solutions, and we also provide an estimate of the first-shell composition.

2.2. Computations. **2.2.1. Density Functional Theory Calculations.** All calculations presented here were performed with the Gaussian09 package (Revision C.1).³² Molecular geometry optimizations for gas-phase metal aqua clusters were carried out with 10 different DFT-based methods. For each optimization, a vibrational analysis was performed to confirm that the geometries correspond to minima on the potential energy surface. The energetic properties of the solvated species were computed without zero-point corrections. The structure of the first coordination sphere of the first-row TM ions in aqueous solution has been well-established as octahedral.³³ However, there is not much structural information available for the second coordination sphere. For a few ions with an octahedral core, 12 water molecules have been found in the second hydration shell.^{34,35} Consequently, the 6 and 18 water models displayed in Figure 1 were taken to model the TM ions involved in the process described by eq 4. These model structures have been successfully used in the past, emphasizing the importance of including the second hydration shell for a more realistic description of bulk solvation.^{36–42}

In accord with the “Jacob’s ladder” to approximate the exact exchange–correlation functional, the 10 DFT-based methods used here can be classified into two main groups, local (or semilocal) and nonlocal. The former group of exchange–correlation functionals can be subdivided into two types, those that depend only on the electron spin density and its gradient (referred to as GGA functionals) and those that incorporate additional local properties such as the kinetic energy density, which are then referred to as meta-GGA (MGGA) functionals. In the latter group, we find that with the same type of functionals (i.e., GGA and MGGA), although with the inclusion of nonlocal effects, there is a certain percentage of exact Hartree–Fock exchange. The former type is referred to as hybrid-GGA (or HGGA), and the latter, hybrid-meta-GGA (or HMGGA) functionals. In the present work, we tested the following 10 functionals: GGAs (BLYP,^{43,44} and PBE⁴⁵), MGGAs (TPSSKCIS,^{46,47} TPSS (TPSS exchange and TPSS correlation functionals),⁴⁷ and M06L⁴⁸), HGGAs (B3LYP^{43,44,49} and PBE0),^{45,50,51} and HMGGAs (M05,⁵² M05-2X,⁵³ and M06⁵⁴). At the same time, these fall into two categories, namely, empirical and nonempirical DFT-based methods. Empirical functionals are based on parameters fitted to standard databases; they are typically more accurate with less systematic errors. Nonempirical functionals are derived from first-principles and theoretical constraints. They can be applied to a range of problems but may exhibit systematic errors for certain types of interactions. The PBE,⁴⁵ PBE0,^{45,50,51} and TPSS⁴⁷ exchange–correlation functionals belong to the latter class of functionals.

We used a double- ζ basis set augmented with d-type polarization and diffuse functions for oxygen and p-type polarization function for hydrogen (i.e., the 6-31+G(d,p) basis set⁵⁵ for water molecules). TM ions were described by an effective core potential (ECP) that replaces 10 core electrons by a semilocal relativistic pseudopotential developed by Dolg and co-workers with their corresponding optimized (8s7p6d1f)/[6s5p3d1f] valence basis set, MDF10,⁵⁶ implemented in Gaussian09.³²

In order to evaluate the performance of the core potential for the prediction of VIEs, AIEs, and λ_o 's, we have also carried out (nonrelativistic) single-point energy calculations using DFT methods combined with the all-electron cc-pVTZ basis set.⁵⁷ The importance of scalar relativistic effects was investigated by carrying out calculations using the all-electron relativistic cc-pVTZ-DK basis set,⁵⁸ applying the Douglas–Kroll–Hess (DKH)^{59,60} second-order scalar relativistic Hamiltonian. For a discussion of these results, we refer to the Supporting Information. Vector relativistic effects, such as spin–orbit interactions, may be significant for compounds containing second- and third-row TM ions.⁶¹ Although a large spin–orbit effect can be expected for bare 3d series TM ions in their electronic ground states because of their high angular and spin moments, Tsushima et al.⁶² showed that the spin–orbit contribution to the gas-phase reaction energy is only 0.2% for the $[\text{Fe}(\text{H}_2\text{O})_6]^{2+}|\text{Fe}(\text{H}_2\text{O})_6]^{3+}$ system. This finding indicates that the presence of water molecules quenches the spin–orbit coupling present in bare 3d cations. Consequently, we did not take this effect into account in the present study.

2.2.2. Solute–Solvent Interactions in Aqueous Solution. Solute–solvent interactions in both vertical and adiabatic ionization processes, eq 4, were described by PCM²⁴ in both the equilibrium (for AIE) and nonequilibrium (for VIE) solvation protocols as implemented in Gaussian09. The equilibrium model accounts for both electronic and nuclear relaxation, whereas the nonequilibrium model accounts for electronic relaxation only. The solvent polarization that is involved in processes with sudden variation of the solute charge distribution is described by dividing it into fast and slow components. The first component is the polarization resulting from the electronic degrees of freedom of the solvent, which will be equilibrated with the charge distribution of the solute in the final electronic state (the oxidized species; right side in eq 4). The second component is the response of the other degrees of freedom (translational, rotational, and vibrational), which will remain equilibrated with the charge distribution of the solute in the initial electronic state (equilibrium geometry of the reduced state; left side in eq 4).

PCM uses the integral equation formalism (IEF–PCM).⁶³ The total solute–solvent interaction energy was obtained using gas-phase geometries for each TM ion in both metal aqua cluster models, with 6 and 18 water molecules. According to the speciation determined in Section 2.1, the inner solvation shell of Ti^{3+} (d^1) includes a chloride counterion, $[\text{TiCl}(\text{H}_2\text{O})_5]^{2+}$. Thus, we have also optimized supersolute models to include a chloride counterion in the first solvation shell for Ti^{3+} as displayed in Figure SI-1. The solvation models have been previously used to compute spectral, electronic, structural, and redox properties as well as hydration enthalpies of aqueous TM ions.^{36–38,41,42} In this study, the cavity around the solute atoms was created using the united-atom universal force field topological model (UFF) atomic radii, which is the default in Gaussian09. The effect of the choice of the cavity radius on the

prediction of VIEs, AIEs, and λ_o 's is discussed in the Supporting Information.

2.2.3. Wave Function Theory Calculations. In order to validate DFT-based methods for predicting VIEs, AIEs, and λ_o 's, we performed some single-point energy calculations using wave function theory (WFT)-based electron correlation techniques. For this purpose, we have employed the second-order Møller–Plesset perturbation theory (MP2⁶⁴) and coupled cluster theory (CCSD(T)⁶⁵) combined at the geometries optimized at the M05-2X/MDF10/6-31+G(d,p) level of theory. MP2 calculations were performed on both cluster models, whereas CCSD(T) calculations were done only on the smallest cluster because they were impractical on the biggest cluster model. The MP2 and CCSD(T) calculations were carried out with the Gaussian09 program.³²

3. DATABASE OF TRANSITION-METAL AQUA IONS

We have chosen to study TM aqua ions for which a wealth of structural data already exists (Table 2). This database contains

Table 2. Experimental M–O Bond Distances (in Angstroms) for Transition-Metal Hexa-Aqua Ions in Aqueous Solution

TM ion	M–O distance	technique	ref
d ¹ Ti ³⁺	2.03	XD ^a	72
d ² V ³⁺	1.99	XD ^a	33
d ³ Cr ³⁺	1.97	EXAFS, LAXS	70
d ⁴ Cr ²⁺	2.17	EXAFS	73
	Mn ³⁺	XD ^a	68
d ⁵ Mn ²⁺	2.20	EXAFS	33
	Fe ³⁺	EXAFS	33
d ⁶ Fe ²⁺	2.12	NS	33
d ⁷ Co ²⁺	2.08	EXAFS	33
d ⁸ Ni ²⁺	2.06	EXAFS	69
d ⁹ Cu ²⁺	2.07	EXAFS, LAXS	74

^aData based on the crystal structure.

11 M–O distances in total, which can be grouped into six and five M–O data for di- and trivalent TM cations, respectively. Some hydrated structures were determined by XD in the solid state,² but structures have been mostly obtained by extended X-ray absorption fine structure (EXAFS),⁶⁶ LAXS,^{7–9} and NS methods.^{10–12} The geometry for Ti³⁺ (d¹), V³⁺ (d²), Cr³⁺ (d³), Mn³⁺ (d⁴), Mn²⁺ (d⁵), Fe³⁺ (d⁵), Fe²⁺ (d⁶), Co²⁺ (d⁷), and Ni²⁺ (d⁸)^{33,67–72} in high-spin states (for those that apply) has been reported to be perfectly octahedral, whereas Cr²⁺ (d⁴) has been established as a Jahn–Teller distorted octahedral configuration.⁷³ For Cu²⁺ (d⁹), two different complexes have been reported, a Jahn–Teller distorted octahedral⁷⁴ and a 5-fold coordination structure.^{75–77} Other ions, such as Ti⁴⁺ (d⁰), V⁴⁺ (d¹), and Cr⁴⁺ (d²), are not included in the database because they form oxo ions in aqueous solution, and TiO²⁺ and VO²⁺ are not included because of their high charge or because diperoxo ions are formed, such as [(H₂O)₃Cr(O₂)₂]²⁺.⁷⁸ There is no experimental evidence of stable Ni³⁺ (d⁷) and Cu³⁺ (d⁸) ions. In spite of the many techniques applied for studying TM ions in condensed phase, there remain many open questions that primarily concern the number of ligands directly coordinated at the TM cation as well as the molecular rearrangement in the second hydration shell.

The database for VIEs consists of 10 experimental measurements for the first-row TM cations, six for divalent and four for trivalent ions, as presented in Tables 1 and 3. In cases where

Table 3. Experimental VIE of 10 TM Ions and ϵ° , AIE, and λ_o of Six Redox Couples in Aqueous Solution

TM ion	VIE (eV)	redox couple	ϵ° (V) ^a	AIE (eV) ^b	λ_o (eV) ^b
d ¹ Ti ³⁺	7.05	Cr ²⁺ Cr ³⁺	−0.407	3.87	2.89
d ² V ³⁺	8.41	Mn ²⁺ Mn ³⁺	1.5415	5.82	3.00
d ³ Cr ³⁺	9.48	Fe ²⁺ Fe ³⁺	0.771	5.05	2.08
d ⁴ Cr ²⁺	6.76	Co ²⁺ Co ³⁺	1.92	6.20	2.50
d ⁵ Mn ²⁺	8.82	Ni ²⁺ Ni ³⁺	2.3	6.58	2.87
	Fe ³⁺	Cu ²⁺ Cu ³⁺	2.4	6.68	2.97
d ⁶ Fe ²⁺	7.13				
d ⁷ Co ²⁺	8.70				
d ⁸ Ni ²⁺	9.45				
d ⁹ Cu ²⁺	9.65				

^aRefs 78–80. ^bThe absolute potential of SHE used is 4.28 eV.

measurements were carried out for different counterions or different concentrations, we have taken into account only samples where the hexa-aqua complex, [M(H₂O)₆]^{q+}, is the majority species, and we report the average VIE for these solutions. The lowest experimental electron binding energy (BE), which corresponds to the HOMO of the metal–aqua complexes, is obtained from the experimental PE spectra.

We have also considered a database of the experimental AIEs. This quantity corresponds to ΔG_{ox}° and can be computed from ϵ° and ΔG_{SHE}° (see eq 2); the latter has been estimated to be 4.28 eV.^{16,17} The AIE database consists of six data, which are also included in Table 3 together with the corresponding ϵ° values.^{79–81} According to Scheme 1, we can also infer the six respective experimental λ_o 's, summarized in Table 3. Some of the oxidized forms of the metal ions (Ti⁴⁺, V⁴⁺, Cr⁴⁺, and Fe⁴⁺) are not stable in aqueous solution and/or form oxo–metal complexes. Their ϵ° values are uncertain and are thus not included in Table 3.

4. RESULTS AND DISCUSSION

4.1. Differential Valence Band PE Spectra. Figure 2 shows a collection of differential valence band PE spectra, from d¹ through d⁹ TM ions, in water. Each individual spectrum was obtained by subtraction of a reference PE spectrum (either a pure water or salt solution with the same counterion concentration as the respective TM solution). For the spectra shown in Figure 2, panels a, b, and d, the reference spectrum was water. For all other PE spectra, the reference spectrum was either MgCl₂ (for all chloride-containing TM salt solutions) or Mg(NO₃)₂ (for all nitrate-containing solutions). These salts were chosen because Mg²⁺ does not have any photoelectron contributions in the valence band region between 5 and 12 eV BE (see Figure SI-2 in the Supporting Information). As an example, the 0.25 m FeCl₂ PE spectrum in Figure 2g results when subtracting the valence band spectrum of a 0.25 m MgCl₂ aqueous solution and thus contains contributions from Fe²⁺ only. The spectra in Figure 2, panels a, b, and d, also contain the counterion signal, Cl[−] 3p, giving rise to the peak at 9.5 eV BE.⁸² The as-measured valence spectra were energy-calibrated using the water peak positions, which are at 11.16 eV (1b₁), 13.5 eV (3a₁), 17.34 eV (1b₂), and 30.9 eV (2a₁).⁸³ Prior to subtraction, the intensities of the measured spectra were normalized to the background signal in the 38–40 eV BE region.

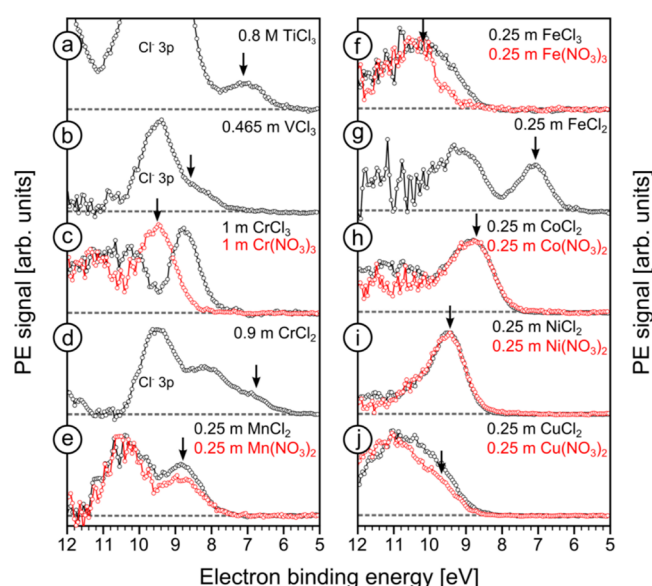


Figure 2. Differential valence photoelectron spectra from $3d^n$, $1 < n < 9$, transition-metal salts in water. Each spectrum was obtained by subtracting a reference spectrum (either from pure water (panels a, b, and d) or from a magnesium salt containing the same counterion concentration as the respective transition metal salt). Black arrows indicate the energy positions of the HOMOs (which equal the VIEs) for the aqua complexes.

In the following sections, we comment on the spectra in Figure 2 in more detail. A summary of all experimental results can be found in Table 1.

4.1.1. Ti^{3+} (d^1). Two peaks at 7.05 and 9.5 eV BE (Figure 2a) are observed below the onset for ionizing neat liquid water. The 9.5 eV peak is due to Cl^- 3p electron emission,⁸² and the weak peak at 7.05 eV represents the HOMO (t_{2g}) of the $Ti^{3+}(aq)$ complex. The approximately 50 times larger signal from Cl^- 3p is mainly due to the larger number of chloride ions in the solution (ca. 7 M Cl^- from HCl versus 2.4 M Cl^- from $TiCl_3$ compared to 0.8 M Ti^{3+}), but it is also due to the fact that there are six electrons in the Cl^- 3p shell, whereas one electron is in the t_{2g} shell of $Ti^{3+}(aq)$. By fitting the spectrum with two Gaussians, we obtain, for the Ti^{3+} peak, a full-width at half maximum (fwhm) of 1.30 eV, which is 0.3–0.4 eV larger than for typical solute fwhm's.^{18,82} This indicates the existence of further species, most probably $[TiCl_2(H_2O)_4]^+$ and $[TiCl(H_2O)_5]^{2+}$.

4.1.2. V^{3+} (d^2). The differential spectrum in Figure 2b can be fitted by two Gaussians with peak positions at 9.60 and 8.41 eV. As for Ti^{3+} , the peak at 9.6 eV is attributed to Cl^- 3p, and we assign the peak at 8.41 eV to the initially doubly occupied t_{2g} level (final state notation, $^2T_{2g}$).

4.1.3. Cr^{3+} (d^3). Figure 2c shows the differential spectra from 1 M hexahydrated $CrCl_3$ (in black) and $Cr(NO_3)_3$ (in red) salts. Both spectra exhibit a distinct peak at the lower BE side, at 8.75 eV for the chloride salt and at 9.54 eV for the nitrate salt. We assign these peaks to initially triply occupied t_{2g} states (final state notation, 3T_1). The shift in energy is clearly related to the different counterions in solution. The lower overall charge of the complex of the majority species in the chloride solution ($[CrCl_2(H_2O)_4]^+$) leads to a lower VIE of the complex compared to the triply charged hexa-aqua complex $[Cr(H_2O)_6]^{3+}$, which is the prevalent species in the nitrate solution. The fwhm of the peak associated with the nitrate

complex (for 1 M concentration) is 1.17 eV (i.e., almost 0.3 eV broader than for the respective 1 M chloride complex). This may be interpreted as a more rigid ligand–metal structure of the $[CrCl_2(H_2O)_4]^+$ complex as compared to that of the hexa-aqua complex.

4.1.4. Cr^{2+} (d^4). Three peaks can be observed in the differential PE spectrum of the 0.9 M solution (Figure 2d). A fit of the spectrum with Gaussians yields peak positions at 9.54, 8.18, and 6.76 eV. As for $TiCl_3$ and VCl_3 , we assign the peak at 9.54 eV to Cl^- 3p. The lower BE peaks correspond to the triply occupied $Cr^{2+}(aq)$ t_{2g} level (8.18 eV; final state, 4T_1) and the singly occupied $Cr^{2+}(aq)$ e_g level (6.76 eV; final state, 4A_2). The area ratio between these two peaks is approximately 3:1, matching the 3:1 ratio of electron occupancy in the t_{2g} and e_g levels. From the fit, we get a rather large margin of error for the fwhm, 1.05 ± 0.13 eV, reflecting the considerable overlap of the HOMO and HOMO-1 states.

4.1.5. Mn^{2+} (d^5). The differential spectra from 0.25 M $MnCl_2$ (in black) and $Mn(NO_3)_2$ (in red) aqueous solutions in Figure 2e exhibit two peaks, at 10.43 and 8.77 eV (chloride salt) and at 10.35 and 8.87 eV (nitrate salt), respectively. These values are in good agreement with our earlier valence band measurements from 0.5 M $Mn(NO_3)_2$, where we found 8.88 eV for the HOMO energy and 10.26 eV for the HOMO-1¹⁹ level. We attribute the slight difference in the intensity of the HOMO peak between the two salt solutions to different counterions in the solution.

4.1.6. Fe^{3+} (d^5). The differential spectra from 0.25 M $FeCl_3$ (in black) and $Fe(NO_3)_3$ (in red) aqueous solutions are shown in Figure 2f. Because the Fe^{3+} signal contribution overlaps entirely with the water $1b_1$ peak, both spectra are noisy. The strong acidity of Fe^{3+} in aqueous solution causes hydrolysis, leading, in the case of a 0.25 M $FeCl_3$ aqueous solution, to a shoulder at ~ 9.2 eV BE and reflecting the OH^- contribution (from $[Fe(H_2O)_5OH]^{2+}$). This shoulder is barely visible in the 0.25 M $Fe(NO_3)_3$ spectrum. When fitting both spectra with two Gaussians, without any constraints, large margins of error occur for the peak positions ($FeCl_3$) as well as for the fwhm. The most accurate value can be given for the HOMO peak for 0.25 M $Fe(NO_3)_3$, 10.28 eV, which is 200 meV higher than that from our recent study on 0.25 M $Fe(NO_3)_3$ in water.²⁰ In the Supporting Information, we show the valence band PE spectra of the higher concentration Fe^{3+} solutions for comparison (Figure SI-3).

4.1.7. Fe^{2+} (d^6). The differential spectrum from 0.25 M $FeCl_2$ exhibits two distinct peaks, at 7.13 eV and around 9.2 eV (Figure 2g). The value for the HOMO peak is in very good agreement with a previous study of this compound, where we found 7.09 eV.²⁰ In that study, a combined experimental–theoretical strategy was carried out, and we argued that the peak at 7.09 eV is due to electron emission from the single beta electron of the t_{2g} level (final state, 6A_1) rather than from the e_g level. This is a consequence of the electron–electron interaction, further reducing the degeneracy of the t_{2g}/e_g manifold as more electrons are filled into the 3d shell.

4.1.8. Co^{2+} (d^7). Figure 2h shows the differential PE spectra from 0.25 M $CoCl_2$ (in black) and $Co(NO_3)_2$ (in red) aqueous solutions. Both spectra exhibit a broad peak at around 8.8 eV, with a long intense tail at higher BE. The similarity between both spectra is an indication that in both cases the first hydration shell environment is very similar. In contrast to the PE spectra shown in Figure 2a–g, the $Co^{2+}(aq)$ spectrum cannot be disentangled into t_{2g} and e_g states without further

information. We sought help from a spectral comparison with cobalt(II) oxide (CoO), arguably the best solid-state analogue of Co^{2+} in water, where the metal cation is also coordinated by six oxygen atoms, giving rise to octahedral symmetry. According to Eastman et al.,⁸⁴ measurements and ligand–field calculations on CoO using the multiplets nomenclature and description from Tanabe, Sugano and Kamimura,⁸⁵ four final states mainly contribute to the PE spectrum. Interestingly, the final state with the lowest energy (and the highest intensity), the $^5\text{T}_2$ state, corresponds to the removal of a $\text{t}_{2\text{g}}$ electron, whereas the second and third lowest states ($^3\text{T}_1$ and $^3\text{T}_2$) correspond to the removal of an e_g electron. Using these assignments, we fitted both spectra in Figure 2h with four Gaussians of the same fwhm. The energy position of the Gaussian with the lowest energy is 8.67 eV for CoCl_2 and 8.72 eV for $\text{Co}(\text{NO}_3)_2$. Although according to speciation calculations, the 1.75 *m* solution is expected to consist mainly of $[\text{CoCl}(\text{H}_2\text{O})_5]^+$, we see no change in either the peak shape or the VIE compared to those of the 0.25 *m* spectrum.

4.1.9. Ni^{2+} (d^8). The PE spectra from 0.25 *m* NiCl_2 (in black) and $\text{Ni}(\text{NO}_3)_2$ (in red) aqueous solutions in Figure 2i are similar to the spectrum from $\text{Co}^{2+}(\text{aq})$, exhibiting a strong peak with an asymmetric tail to the higher BE side. As for Co^{2+} , we refer to the literature in determining the underlying structure. Ligand–field calculations of NiO identify three final states in the low-energy part of the valence band, ranked from low to high energy: $^4\text{T}_1$ (electron removal from $\text{t}_{2\text{g}}$), ^2E (e_g), and $^2\text{T}_1$ ($\text{t}_{2\text{g}}$).⁸⁴ Fitting our spectrum by three Gaussians gave an energy value between 9.41 and 9.48 eV for the lowest peak position (which equals VIE) of all nickel salts that we measured.

4.1.10. Cu^{2+} (d^9). We present in Figure 2j the differential spectra from 0.25 *m* CuCl_2 (in black) and $\text{Cu}(\text{NO}_3)_2$ (in red) aqueous solutions. Both spectra show a broad structure but are slightly different in shape, which is due to different first solvation shells. Speciation effects are even more distinct for the higher concentration solutions from 1.75 *m* CuCl_2 and 2 *m* $\text{Cu}(\text{NO}_3)_2$ (see spectra in Figure SI-4). Fitting the spectrum with three Gaussians, representing the most intense final states $^3\text{A}_2$, $^3\text{T}_2$, and $^3\text{T}_1$, yields the lowest BE of approximately 9.6 eV for both salt solutions. The broad PE structure may reflect the strong fluctuations of the Cu^{2+}_aq ion between a distorted octahedron/square pyramid and a 5-fold coordinated trigonal bipyramidal structure as suggested in refs 75 and 76.

Overall, the VIEs from chloride-containing TM solutions are generally lower in energy compared to their nitrate counterparts, implying that the aqua complex is more favorable in solutions where nitrate is the counterion.

4.2. Trends from Experimental Data. Figure 3 shows a plot of the VIE for each d system. In the case of Cr^{3+} , Fe^{3+} , and Cu^{2+} , values are given only for the aqua complex. In the following we rationalize the observed trends qualitatively by considering ligand field theory, exchange interactions and the total charge of the ions. Taking the BE of 7.05 eV for $\text{Ti}^{3+}(\text{aq})$ d^1 as a starting point, we expect an increase in the VIE for $\text{V}^{3+}(\text{aq})$ d^2 because there are two electrons in the $\text{t}_{2\text{g}}$ level (but only one for Ti^{3+}), which leads to a higher stabilization energy (−8 Dq for V^{3+} compared to −4 Dq for Ti^{3+}). The more negative the Dq value, the higher the stabilization energy and the higher the VIE. The absolute value for Dq depends on the ligand, the metal ion, and strongly on the oxidation state. A higher oxidation state leads to a decrease in the distance between the metal ion and its surrounding ligands, resulting in an increase of the ligand–field strength. For $\text{Ti}^{3+}(\text{aq})$ and

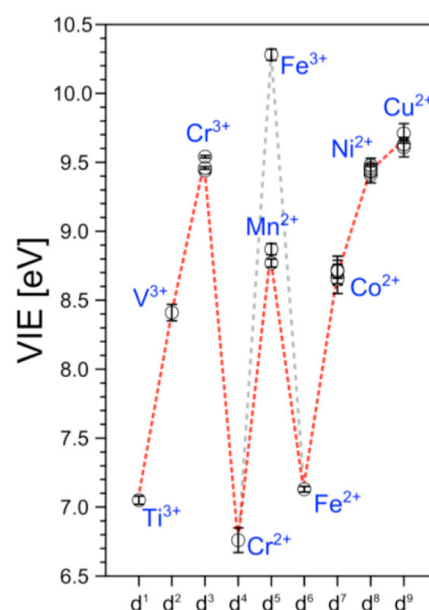


Figure 3. Experimental VIEs as a function of d occupancy for $\text{TM}^{2+/3+}(\text{aq})$. All values are for the hexa-aqua complex. (See Table 1.)

$\text{V}^{3+}(\text{aq})$, the ligand–field strength is approximately the same, 0.25 and 0.27 Dq (eV), respectively.⁸⁶ In fact, $\text{V}^{3+}(\text{aq})$ has a VIE of 8.41 eV, which is 1.36 eV larger than that for Ti^{3+} . Another factor contributing to the ligand–field stabilization is that the additional nuclear charge is not fully screened by the additional electron when filling a given shell in going from left to right in the periodic table. Hence, more energy is required to remove an electron from the TMs further right in the periodic table.

For $\text{Cr}^{3+}(\text{aq})$ (d^3), two effects should lead to an even higher VIE: the half-filled shell effect (i.e., the three electrons in the $\text{t}_{2\text{g}}$ orbital result in a high stabilization energy of −12 Dq) and the exchange interaction between three electrons with the same spin, which is larger than for $\text{V}^{3+}(\text{aq})$ with its two valence electrons. The more electrons with the same spin orientation, the greater the exchange interaction and thus the stabilization, resulting in a higher VIE. In fact, we measured the VIE for $\text{Cr}^{3+}(\text{aq})$ to be ~9.5 eV, which is 1.1 eV larger than that for $\text{V}^{3+}(\text{aq})$, consistent with our predictions.

The fourth d electron in $\text{Cr}^{2+}(\text{aq})$ (d^4) occupies the e_g level and has the same spin orientation as the three $\text{t}_{2\text{g}}$ electrons (high-spin complex). Therefore, the exchange interaction of $\text{Cr}^{2+}(\text{aq})$ is even larger than that for $\text{Cr}^{3+}(\text{aq})$, but the ligand–field stabilization is now decreased to −6 Dq, and the oxidation state is changed from +3 to +2. The latter two effects lead to destabilization (lower VIE) and are expected to overcome the stabilization effect from the exchange interaction. In fact, we measure a VIE of 6.76 eV for $\text{Cr}^{2+}(\text{aq})$ (i.e., approximately 2.75 eV lower than that for $\text{Cr}^{3+}(\text{aq})$).

$\text{Mn}^{2+}(\text{aq})$ (d^5) has a half-filled shell with five electrons (two in e_g and three in $\text{t}_{2\text{g}}$) with the same spin, resulting in an even higher exchange interaction compared to that of $\text{Cr}^{2+}(\text{aq})$ but with less ligand–field stabilization (0 Dq). Because the oxidation state remains the same, the exchange interaction dominates over the ligand–field destabilization. Therefore, we expect a higher VIE for $\text{Mn}^{2+}(\text{aq})$ compared to that of $\text{Cr}^{2+}(\text{aq})$, and this has indeed been measured, ~8.8 eV compared to 6.76 eV for $\text{Cr}^{2+}(\text{aq})$.

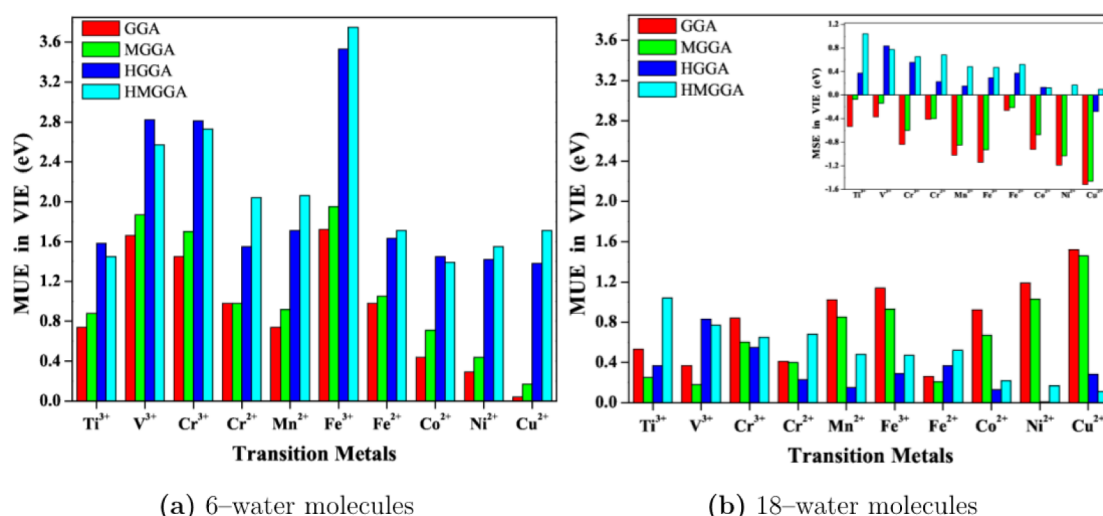


Figure 4. Mean unsigned error (MUE) of VIE (in electron volts) for the (a) $[M(H_2O)_6]^{q+}$ and (b) $[M(H_2O)_{18}]^{q+}$ cluster models. Ti^{3+} is modeled as $[TiCl(H_2O)_{n-1}]^{2+}$ ($n = 6, 18$). The inserted graphic shows the mean signed error (MSE) of VIE. The average is taken over each functional category: GGA (red), MGGA (green), HGGA (dark blue), and HMGGA (light blue). Errors of the M05-2X functional are not included for HMGGA-type.

Although $Fe^{3+}(aq)$ (d^5) has the same spin configuration as $Mn^{2+}(aq)$, the ligand–field strength is much larger because of the higher oxidation state (and therefore the VIE), which is confirmed by our measurements, ~ 10.3 eV for the VIE, approximately 1.5 eV higher than that for $Mn^{2+}(aq)$.

The d^6 system $Fe^{2+}(aq)$ should have a lower VIE compared to $Fe^{3+}(aq)$, as the oxidation state is reduced, even though the ligand–field stabilization energy is $-4 Dq$ ($0 Dq$ for Fe^{3+}). Furthermore, the sixth electron is sharing the same orbital with one of the t_{2g} electrons, forming an electron pair with different spins. This leads to a destabilization, as the average distance between electrons with different spins is closer than the distance between electrons with the same spin, resulting in stronger electron–electron repulsion (decreasing the VIE). The measured VIE of $Fe^{2+}(aq)$ is ~ 7.1 eV (i.e., approximately 3.2 eV lower than that for $Fe^{3+}(aq)$ and still 1.7 eV lower than that for $Mn^{2+}(aq)$).

$Co^{2+}(aq)$ (d^7) and $Ni^{2+}(aq)$ (d^8) have the same oxidation state as $Fe^{2+}(aq)$, but they gain a higher stabilization from the ligand–field ($-8 Dq$ for Co^{2+} and $-12 Dq$ for Ni^{2+}) and from the exchange interaction. Only the higher number of electron pairs (two for Co^{2+} and three for Ni^{2+}) counteracts these effects. Overall, we expect an increase in the VIE for $Co^{2+}(aq)$ and an even larger increase for $Ni^{2+}(aq)$ compared to that of $Fe^{2+}(aq)$, which was confirmed by our measurements. The VIEs of $Co^{2+}(aq)$ and $Ni^{2+}(aq)$ are ~ 1.6 and ~ 2.3 eV larger than that for $Fe^{2+}(aq)$.

$Cu^{2+}(aq)$ (d^9) is a special case, as one cannot unequivocally predict whether it will have a higher or lower VIE than $Ni^{2+}(aq)$. On one hand, the exchange interaction is highest among all systems studied here, leading to a high stabilization energy (i.e., higher VIE); on the other hand, the stabilization energy from the ligand field is lower compared to those of $Ni^{2+}(aq)$ and $Co^{2+}(aq)$. Furthermore, there are four electron pairs, which should also reduce the VIE. Our measurements reveal a slightly higher VIE compared to $Ni^{2+}(aq)$, approximately 9.6 eV, which is 0.15 eV higher.

4.3. Calculations. **4.3.1. Molecular Structure.** Geometry optimizations for gas-phase metal–aqua complexes were carried out in their high-spin states. Although crystal field theory helps to explain the multiplicity of hexahydrated 3d ions, in some

cases the ion may be more stable in a different spin state. For those systems where the spin ground state is not clearly known, as for $Co^{2+/3+}$ and Ni^{3+} , we optimized low- and high-spin states, and we found that the latter is the most stable, even though experiments reveal $[Co(H_2O)_6]^{3+}$ as a low-spin complex. All computed structures were confirmed as true minima on the potential energy surface through vibrational analysis. The M–O bond lengths obtained are summarized in Tables SI-1 and SI-2 in the Supporting Information. We found that by including a second explicit water shell (18 vs 6 water model), the mean unsigned error over all functional classes and ions is significantly reduced from 0.041 to 0.028 Å. HMGGA functionals are the most accurate (M05-2X, MUE = 0.013 Å), followed, in order, by HGGA (PBE0, MUE = 0.016 Å), MGGA (M06L, MUE = 0.023 Å), and GGA (PBE, MUE = 0.034 Å). A more detailed discussion of the performance of the functionals and the 6 and 18 water models for predicting the structure of di- and trivalent ions can be found in the Supporting Information.

4.3.2. Vertical Ionization Energy. $[M(H_2O)_6]^{q+}$. Calculated VIEs of hydrated TM ions and the lowest experimental ionization energies from the HOMO level are collected in Table SI-3 (see Supporting Information), along with MUE and AMUE (which were defined in Section 4.3.1 and are used to evaluate the functionals' performance). The comparison with experimental data shows that the VIEs of the 10 TM complexes are all overestimated by all DFT functionals. Considering the mean unsigned errors of each functional category averaged over all metals (AMUE), we find the following results. Incorporation of a certain percentage of exact Hartree–Fock exchange generates errors in VIEs that are almost twice as large as those for nonhybrid functionals (AMUE of 0.90 and 1.07 eV for GGA and MGGA, respectively, against 1.99 and 2.35 eV for HGGA and HMGGA, respectively). Overall, the best performing functional family is GGA (BLYP (0.90 eV) and the nonempirical DFT-based method, PBE (0.91 eV)), and the worst is HMGGA (M05 (2.20 eV) and M05-2X (2.85 eV)).^{53,87,88} In previous reports, it has indeed been shown that functionals with a high percentage of exact Hartree–Fock exchange (e.g., M05-2X) are not suitable to predict energetic properties in TM-containing molecules.⁵³ Despite the fact that

M05-2X with the smaller hydration model is the worst performing DFT-based method in predicting VIEs, it is the best suited functional in predicting M–O bond lengths for the whole set of 10 TM ions. For our purpose, M05-2X will not be treated as a representative functional in the HMGGA category in the following discussions; yet, results are included in the respective tables. Finally, Table SI-3 of the Supporting Information shows that if the incorrect hexaqua coordination model is employed for Ti^{3+} (i.e., without a Cl^- counterion) then the incurred errors in the predicted VIEs increase by about 1.3 eV independent of the DFT functional.

Figure 4a presents the predicted MUE of VIEs (for all functionals except for M05-2X) for the set of TM complexes. Calculations with hybrid-type functionals exhibit large errors for the 6 water model, and they are also quite inaccurate for trivalent ions, which have the greatest MUE, approximately 2.66 eV, an average over the two hybrid categories against 1.52 eV for nonhybrid categories (GGA-MGGA). The latter failure arises because even though the high positive charge on both states, reduced (trivalent) and oxidized (tetravalent), has been delocalized throughout the water molecules, the supersolute model is not big enough to effectively produce charge delocalization. Therefore, the charge localized on the hydrogen atoms (ca. 1.7 and 2.7 w.r.t. V^{3+} and V^{*4+} , respectively; see atomic charges in Table SI-7) is very large causing the so-called first solvation shell effects.^{25,26} If the local electric field in the vicinity of the solute is very high, the modeling of the solvent by a bulk dielectric continuum becomes less accurate. This phenomenon implies fictitious solute–solvent interactions that lead to overstabilized solutes as a consequence of the overestimated dielectric response by continuum treatment. The effect is more significant for compact structures, where the charge is slightly more confined on the metal, as compared to those found using hybrid-type functionals (see Table SI-1). Finally, for the divalent subset, we note that only the VIEs of Mn^{2+} , Co^{2+} , Ni^{2+} , and Cu^{2+} are estimated with errors less than 1 eV for the GGA and MGGA methods and that once again the hybrid functional families exhibit the greatest MUE (ca. 1.63 eV averaged over both hybrid categories against 0.66 eV for the local and semilocal families).

$[\text{M}(\text{H}_2\text{O})_6]^{q+}$. The results are presented in Figure 4b and Table SI-4. In contrast to the 6 water model, for which VIEs are overestimated by all functionals, for the 18 water model, the errors can go in either direction. This is seen in the inset of Figure 4b, which contains the mean signed errors (MSE). When the second hydration shell is included, the GGA and MGGA functionals underestimate VIE for all 10 TM ions, whereas HGGA and HMGGA overestimate VIE for Ti through Ni. Cu^{2+} is both underestimated and overestimated by the HGGA and HMGGA functionals, respectively.

A comparison of panels a and b in Figure 4 clearly shows that inclusion of the second hydration shell leads to more accurate results, reducing the AMUE, taken over all metals, from 0.90, 1.07, 1.99, and 2.10 eV for the 6 water models to 0.82, 0.67, 0.32, and 0.44 eV for the GGA, MGGA, HGGA, and HMGGA functional families, respectively. Overall, the HGGA family gives the best performance for all 10 TM ions. Notably, improvements for trivalent ions are about 50% independent of the DFT functional as well as for hybrid-type methods, which predict VIE errors of less than 0.9 eV for all 10 TMs. In the case of the divalent subset, local and semilocal functionals yield the greatest MUE, ca. 0.82 eV versus 0.28 eV, for hybrid categories. Of the tested DFT-based methods, the most accurate one for

trivalent ions is the MGGA functional, M06L, whereas the HGGA functional, PBE0, performs best for divalent ions. Notice that the VIE values for divalent ions are strongly underestimated by nonhybrid functionals, whereas they are moderately overestimated by hybrid functionals. Nonhybrid functional accuracies diminish when the second coordination sphere is included with the exception of Cr^{2+} and Fe^{2+} .

The remarkable improvements obtained for the 18 water model, especially for trivalent ions, are due to the more effective charge delocalization before and after ionization, respectively, throughout the larger supersolute model. For example, the amount of positive charge localized on the second solvation shell in the 18 water model is ca. 1.2 and 1.8 for V^{3+} and V^{*4+} , respectively, compared to approximately 1.7 and 2.7 for the first solvation shell of the 6 water model (see atomic charges in Table SI-7). These reductions on the positive charge localized on the interface between explicit water and continuum, which are more pronounced for oxidized ions, imply a smaller first solvation shell effect (i.e., supersolute–solvent (bulk–dielectric continuum) electrostatic interactions are more realistically accounted for with the inclusion of the second hydration shell and therefore the solvation energies are less overestimated).

In order to confirm our DFT-based predictions of VIEs, we performed single-point energy calculations using WFT-based methods: Hartree–Fock (HF), second-order Møller–Plesset perturbation theory (MP2), and coupled clusters CCSD(T). The results are summarized in Tables SI-5 and SI-6 (Supporting Information). As can be seen in Table SI-5, the errors resulting from the inclusion of electron correlation in the MP2 and CCSD(T) calculations can go in either direction relative to those from the HF results, which, in contrast, gave the smallest AMUE. For the 6 water model, the calculated VIEs of trivalent TM aqua complexes are too low at the MP2 and CCSD(T) levels (except for Ti^{3+} with counterion Cl^-), whereas the opposite is found for the hydrated divalent TM ions. The trend is the same for the 18 water models (see Table SI-6) except for Fe^{3+} and Cu^{2+} . Overall, WFT-based methods have larger AMUEs than the best DFT-based calculations. It should be emphasized that the AMUE of WFT-based methods are reduced by about 47 and 60% at the HF and MP2 levels when the second hydration is explicitly treated.

4.3.3. Atomic Charges. The extent of charge delocalization was investigated by calculating the natural atomic charges (NBO)⁸⁹ for both cluster models and for one functional per category (BLYP, M06L, B3LYP, and M06). These values are reported in Table SI-7 of the Supporting Information. In Figure SI-6, we show the difference in atomic charges between the reduced and oxidized states, respectively, $\Delta q = q(\text{M}(\text{aq})^{*(q+1)+}) - q(\text{M}(\text{aq})^{q+})$. The charge differences are broken down into contributions from the metal center (M^{q+}), the first hydration shell, and the second hydration shell. We find that the results are rather insensitive to the type of functional used. For both supersolute models, most of the positive charge difference is delocalized over the water molecules; the first hydration shell in both trivalent and divalent TM ions reaches more than 80% for the former and 65% for the latter. Therefore, if these positive charges are confined to more compact clusters, then the oxidized states will be concomitantly destabilized, which is the case for hybrid-type functionals that are best suited for the smaller M–O bond distances and higher VIEs.

4.3.4. Adiabatic Ionization Energy. The AIEs obtained for $[\text{M}(\text{H}_2\text{O})_6]^{2+}$ and $[\text{M}(\text{H}_2\text{O})_{18}]^{2+}$ supersolutes are compiled in Table SI-6 (Supporting Information) together with the

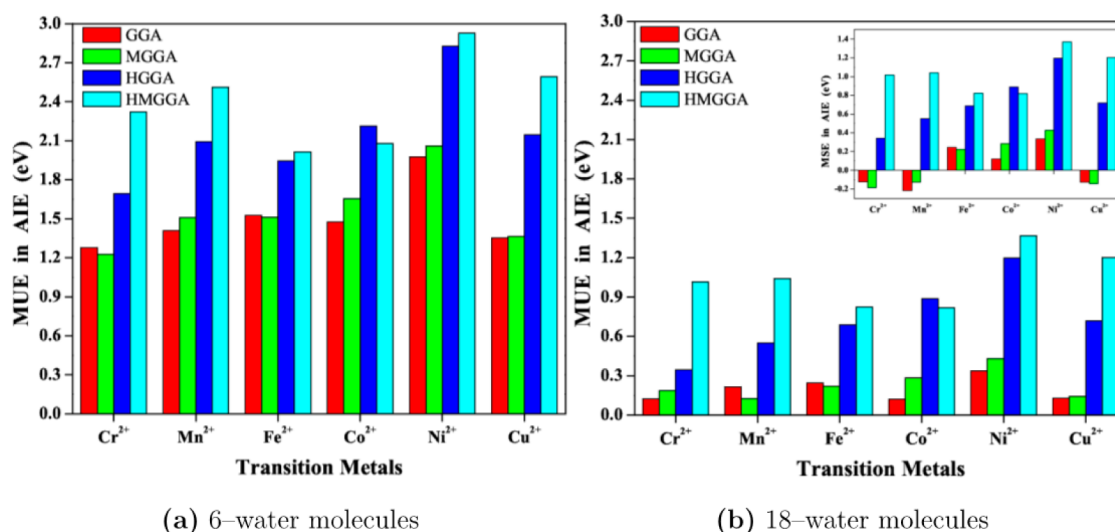


Figure 5. Mean unsigned error (MUE) of AIE (in electron volts) for the (a) $[M(H_2O)_6]^{2+}$ and (b) $[M(H_2O)_{18}]^{2+}$ cluster models. The inset in panel b shows the mean signed error (MSE) of AIE. The average is taken over each functional category: GGA (red), MGGA (green), HGGA (dark blue), and HMGGGA (light blue). Errors of the M05-2X functional are not included for HMGGGA-type.

experimental data (considering a value of 4.28 eV^{16,17} for SHE). Again, the MUE and AMUE are also included in Table SI-8, and the former are displayed in Figure 5 except for the M05-2X functional, which performs the worst in predicting AIEs and is thus not included in the following discussion. However, it is considered in Table SI-8.

$[M(H_2O)_6]^{2+}$. Comparison with experimental data reveals that AIEs are strongly overestimated by all functionals, especially by those with a certain percentage of exact Hartree–Fock exchange (Figure 5a). As can be inferred from Table SI-8 and Figure 5, the GGA family is the best in predicting AIEs (BLYP) with an AMUE, averaged over all metals, of 1.50 eV; this is closely followed by MGGA (1.55 eV), with the nonempirical PBE and TPSS functionals showing the same performance. Both hybrid families are the least accurate, with 2.15 and 2.41 eV for HGGA and HMGGGA, respectively, with M05 being the least accurate functional. The highly overestimated AIEs can be rationalized in terms of overstabilized solutes, as was done for VIE. The 6 water model does not effectively delocalize the positive charges, implying interactions with the continuum solvent that may deviate significantly from that expected for a bulk–dielectric continuum. The effectiveness in charge delocalization can be seen in Table SI-7, and the analysis is quite similar to that presented in Section 4.3.2 for VIEs.

$[M(H_2O)_{18}]^{2+}$. Calculated AIEs are reported at the right side of Table SI-8 in the Supporting Information. Comparing panels a and b in Figure 5, it can be noticed that the inclusion of the second hydration shell greatly improves the estimate of AIE, reducing the errors by at least 60%. Looking at the AMUE in Table SI-8 for each functional family, the order of performance in predicting AIEs is the same as that for the smaller hydration model. The best is GGA (0.19 eV), which is closely followed by MGGA (0.23 eV) and then by HGGA and HMGGGA (0.73 and 1.04 eV). Overall, the most accurate functional for AIEs is the local PBE (a nonempirical type), with an AMUE of 0.18 eV (equal to 180 mV in the prediction of standard oxidation potential), which is smaller than that for both BLYP and TPSSKCIIS by 0.03 eV and for TPSS (a nonempirical type) by 0.05 eV. Once again, the M05 functional is the least accurate

method, with an AMUE value of 1.23 eV. The improved results for the 18 water model can be explained in terms of both the quality of the gas-phase geometry of the reduced and oxidized states and the improved electronic and nuclear relaxation within the equilibrium solvation model. Comparison with experimental data shows that only Cr^{2+} , Mn^{2+} , and Cu^{2+} energies are slightly underestimated for the GGA and MGGA families (see the inset of Figure 5b, which contains the mean signed errors, MSE).

It is interesting to note that Ni^{2+} exhibits a higher MUE than the other TM ions independent of the DFT functional and of the supersolute model. This larger error could be due to a less certain experimental AIE reference value, which, in accordance with eq 2, arises from an uncertain standard reduction potential (2.3 V) (i.e., from a value with fewer significant digits), implying smaller reliability. Furthermore, according to Tables SI-1 and SI-2 of the Supporting Information, the geometry for Ni^{2+} is well-described, whereas experimental data for Ni^{3+} is not available. The large error could thus be indicative of a wrong molecular structure (i.e., 5-fold rather than 6-fold coordination). This is indicated by the frequency calculations; it is well-known that the vibrational energy of the fundamental mode increases with the charge state of the ion. However, the redox couple $Ni^{2+/3+}$ is the only one for which the zero-point energy is greater for the reduced species than for the oxidized one.

It should be also mentioned that the AMUE values quoted in Table SI-8 depend on the choice of the reference value for the absolute SHE. Here, we have taken a reference value of 4.28 eV,^{16,17} but other estimates are used in the literature, 4.44⁹⁰ or 4.36 eV.¹⁶ Taking the latter values would give slightly reduced errors.

As can be seen in Tables SI-5 and SI-6, again, the WFT-based methods are less accurate for predicting AIEs than local or semilocal DFT-based methods. Overall, the WFT-based performance may be compared to nonlocal exchange–correlation functionals (HGGA and HMGGGA for the 6 water model and HMGGGA for the 18 water model). Here, a second shell effect is also observed, and the errors are reduced by about 45 and 60% at the HF and MP2 levels, respectively.

Table 4. Best Three DFT Methods Recommended for Computation of Geometry, Vertical and Adiabatic Ionization Energies, and Reorganization Energy

cluster model	charge ion	M–O bond length	VIE	AIE	λ_o
$[M(H_2O)_6]^{q+}$	trivalent	M06	PBE		
		M05-2X	BLYP		
		PBE0	TPSSKCIS		
	divalent	M05-2X	BLYP	BLYP	M05-2X
		M06	PBE	PBE	PBE0
		PBE0	TPSSKCIS	TPSS	M06
	all ions	M05-2X	BLYP	BLYP	M05-2X
		M06	PBE	PBE	PBE0
		PBE0	TPSSKCIS	TPSS	M06
	$[M(H_2O)_{18}]^{q+}$	trivalent ^a	M06		
			M05-2X		
			PBE0		
	divalent	M05-2X	PBE0	PBE	M05-2X
		PBE0	B3LYP	TPSSKCIS	PBE0
		M06	M06	BLYP	M06
	all ions	M05-2X	B3LYP	PBE	M05-2X
		M06	M06	TPSSKCIS	PBE0
		PBE0	PBE0	BLYP	M06

^aTi³⁺ values with Cl[−] counterion.

4.3.5. Single-Ion Reorganization Free Energy. As depicted in Scheme 1, the single-ion reorganization free energy of the oxidized TM ion, λ_o , is the difference between VIE and AIE. The predicted values are listed in Table SI-9 together with experimental energies, MUEs, and AMUEs for the six TM couples.

$[M(H_2O)_n]^{2+/3+}$ ($n = 6, 18$). All predicted values for λ_o are lower than experimental ones independent of the DFT functional and cluster model. Comparing the AMUE of the four functional families, it can be noticed that errors are almost the same irrespective of the cluster model ($n = 6, 18$). Furthermore, the comparison also shows that incorporation of a certain percentage of exact Hartree–Fock exchange leads to a reduction in λ_o errors by about 32 and 27% with respect to the GGA and MGGA functionals, respectively, for both the 6 and 18 water models. Despite these improvements, only the Cr^{2+/3+} redox couple is predicted to be within less than 10% error for both hybrid- and non-hybrid-type (≈ 0.20 and ≈ 0.26 eV, respectively), whereas all functionals are unsuitable in predicting λ_o for Ni^{2+/3+}. Here, values are more than 40% (≈ 1.3 eV) larger than experimental values. Overall, M05-2X (a HMGGA functional) is performing the best, whereas both GGA functionals, BLYP and PBE, cannot predict λ_o well enough.

The large underestimation of reorganization free energy irrespective of the functional used implies that the structural reorganization of the solvation shell upon ionization is not adequately accounted for by the continuum solvation model used. For instance, the structural changes in the second solvation shell are likely to be much more pronounced than what we obtained by simple geometry optimizations, and the number of water molecules in the second solvation shell may change as well in response to ionization. In previous works, we have also noticed that higher solvation shells and bulk solvent significantly contribute to reorganization free energy.^{22,91,92} This effect may be underestimated by the continuum model used. Clearly, DFT-based molecular dynamics simulations would give a more realistic description of solvent fluctuations and reorganization free energy,^{19,22,93} but such simulations are

computationally highly demanding and cannot be carried out to test the performance of a large set of functionals on a series of TM ions as was done in the present work.

The AMUEs of the WFT-based methods are in the range of the DFT-based results, as can be seen in Tables SI-5 and SI-6 for the 6 and 18 water clusters.

5. CONCLUDING REMARKS

We have found that the lowest VIE of all TM complexes studied here is smaller than the lowest VIEs of water. In other words, the highest occupied molecular orbital of the TM–aqua complexes is above the valence band of liquid water. One exception is Fe³⁺, where VIE overlaps with the water valence band.

We have presented a detailed study of the performance of various exchange–correlation functionals (GGA, HGGA, MGGA, and HMGGA) for predicting geometry, vertical and adiabatic ionization energies, and reorganization free energy for first-row TM (Ti through Cu) aqua complexes using two supersolute models: $[M(H_2O)_6]^{q+}$ and $[M(H_2O)_{18}]^{q+}$. Overall, the accuracy of 10 DFT-based methods combined with the MDF10(ECP)/6-31+G(d,p) basis set was assessed for 11 M–O bond distances, 10 vertical ionization energies measured by liquid microjet photoelectron spectroscopy, and 6 adiabatic ionization energies from electrochemical measurements and from their reorganization free energies. From our assessment summarized in Table 4, the following guidelines for TM–ion aqua complexes can be proposed:

- (I) The HGGA and HMGGA functionals, M05-2X, M06, and PBE0, are recommended for geometry optimizations of TM–aqua complexes. M05-2X and M06 are empirical functionals, whereas PBE0 is based on a nonempirical PBE functional including 25% exact Hartree–Fock exchange.
- (II) For VIEs using the most realistic 18 water model, the HGGA and HMGGA functionals (e.g., PBE0, B3LYP, and M06) perform the best for divalent aqua complexes, whereas the MGGA functional, M06L, shows the best performance for trivalent cations. The “good” perform-

ance of the GGA functionals (PBE and BLYP) for the 6 water model is the result of error cancellation: the tendency of the GGA functionals to predict VIEs that are too low is partly compensated by an insufficient number of explicit water molecules.

- (III) For both cluster sizes, it was found that nonhybrid functionals (e.g., PBE, BLYP, TPSS, and TPSSK CIS) show the best performance for AIEs. Values improve for the larger cluster size. However, this again is likely to be a consequence of error cancellation. If reorganization free energy were equal to experimental values (see IV below), then AIEs would be underestimated with GGAs and AIEs would be better described with hybrid functionals.
- (IV) Errors in reorganization free energies are large for both small and large cluster sizes and for all functionals (HGGA gives the best results). When using cluster models, improved sampling of cluster configurations is necessary. The method of choice is DFT-based MD in combination with finite system size corrections (see refs 19–22).
- (V) Finally, we conclude that the explicit inclusion of the second hydration shell (18 water model) is necessary to obtain reasonable estimates of M–O bond distances, VIEs, and AIEs for TM ions in water.

■ ASSOCIATED CONTENT

■ Supporting Information

Description of the preparation of TM aqueous solutions; aquachloro supersolute models $[\text{TiCl}(\text{H}_2\text{O})_{n-1}]^{2+}$ $n = 6, 18$ used to predict VIE; valence PE spectrum of MgCl_2 aqueous solution and differential valence PE spectra of FeCl_3 and CuX_2 ($\text{X} = \text{Cl}, \text{NO}_3$), respectively; discussion of the performance of DFT- and WFT-based methods for predicting M–O distances, VIE, AIE, and λ_o ; MUEs and AMUEs; and discussion of technical aspects such as basis set effects and cavity radii models. This material is available free of charge via the Internet at <http://pubs.acs.org>.

■ AUTHOR INFORMATION

Corresponding Authors

*(B.W.) E-mail: bernd.winter@helmholtz-berlin.de; Phone: +30-8062-15001.

*(J.B.) E-mail: j.blumberger@ucl.ac.uk; Phone: +44-(0)20-7679-7145.

*(P.J.) E-mail: pjaque@unab.cl; Phone: +56-2-27703218.

Author Contributions

[†]Equal contribution of D.Y. and R.S.

Notes

The authors declare no competing financial interest.

■ ACKNOWLEDGMENTS

The authors acknowledge FONDECYT through project no. 1100291 and Millenium Nucleus CPC grant NC120082. P.J. thanks the Universidad Andres Bello for the continuous support of his research group. D.Y. thanks CONICYT for a Ph.D. scholarship and Universidad Andres Bello for support through grant DI-09-11/I. J.B. thanks the Royal Society for a University Research Fellowship. The authors thank the BESSY II staff for assistance, and R.S. acknowledges support from the German Research Foundation (SE 2253/1-1).

■ REFERENCES

- (1) Marcus, Y. Effect of Ions on the Structure of Water: Structure Making and Breaking. *Chem. Rev.* **2009**, *109*, 1346–1370.
- (2) Head-Gordon, T.; Hura, G. Water Structure from Scattering Experiments and Simulation. *Chem. Rev.* **2002**, *102*, 2651–2669.
- (3) Dillon, S. R.; Dougherty, R. C. Raman Studies of the Solution Structure of Univalent Electrolytes in Water. *J. Phys. Chem. A* **2002**, *106*, 7647–7650.
- (4) Fecko, C. J.; Eaves, J. D.; Loparo, J. J.; Tokmakoff, A.; Geissler, P. L. Ultrafast Hydrogen-Bond Dynamics in the Infrared Spectroscopy of Water. *Science* **2003**, *301*, 1698–1702.
- (5) Marechal, Y. Observing the Water Molecule in Macromolecules Using Infrared Spectrometry: Structure of the Hydrogen Bond Network and Hydration Mechanism. *J. Mol. Struct.* **2004**, *700*, 217–223.
- (6) Nibbering, E. T. J.; Elsaesser, T. Ultrafast Vibrational Dynamics of Hydrogen Bonds in the Condensed Phase. *Chem. Rev.* **2004**, *104*, 1887–1914.
- (7) Wilson, K. R.; Cavalleri, M.; Rude, B. S.; Schaller, R. D.; Nilsson, A.; Pettersson, L. G. M.; Goldman, N.; Catalano, T.; Bozek, J. D.; Saykally, R. J. Characterization of Hydrogen Bond Acceptor Molecules at the Water Surface Using Near-Edge X-ray Absorption Fine-Structure Spectroscopy and Density Functional Theory. *J. Phys.: Condens. Matter* **2002**, *14*, L221–L226.
- (8) Kashtanov, S.; Augustsson, A.; Luo, Y.; Guo, J. H.; Sathe, C.; Rubensson, J. E.; Siegbahn, H.; Nordgren, J.; Agren, H. Local Structures of Liquid Water Studied by X-ray Emission Spectroscopy. *Phys. Rev. B* **2004**, *69*, 024201.
- (9) Smith, J. D.; Cappa, C. D.; Wilson, K. R.; Messer, B. M.; Cohen, R. C.; Saykally, R. J. Energetics of Hydrogen Bond Network Rearrangements in Liquid Water. *Science* **2004**, *306*, 851–853.
- (10) Quirke, N.; Soper, A. K. Neutron Scattering from $\text{NiCl}_2/\text{D}_2\text{O}$ – A Hard-Sphere Approach. *J. Phys. C: Solid State Phys.* **1977**, *10*, 1803–1807.
- (11) Leberman, R.; Soper, A. K. Effect of High Salt Concentrations on Water Structure. *Nature* **1995**, *378*, 364–366.
- (12) Botti, A.; Bruni, F.; Imberti, S.; Ricci, M. A.; Soper, A. K. Ions in Water: The Microscopic Structure of a Concentrated HCl Solution. *J. Chem. Phys.* **2004**, *121*, 7840–7848.
- (13) Thurmer, S.; Seidel, R.; Eberhardt, W.; Bradforth, S. E.; Winter, B. Ultrafast Hybridization Screening in Fe^{3+} Aqueous Solution. *J. Am. Chem. Soc.* **2011**, *133*, 12528–12535.
- (14) Thurmer, S.; Seidel, R.; Winter, B.; Oncak, M.; Slavicek, P. Flexible H_2O_2 in Water: Electronic Structure from Photoelectron Spectroscopy and Ab Initio Calculations. *J. Phys. Chem. A* **2011**, *115*, 6239–6249.
- (15) Seidel, R.; Ghadimi, S.; Lange, K. M.; Bonhommeau, S.; Soldatov, M. A.; Golnak, R.; Kothe, A.; Konnecke, R.; Soldatov, A.; Thurmer, S.; et al. Origin of Dark-Channel X-ray Fluorescence from Transition-Metal Ions in Water. *J. Am. Chem. Soc.* **2012**, *134*, 1600–1605.
- (16) Lewis, A.; Bumpus, J. A.; Truhlar, D. G.; Cramer, C. J. Molecular Modeling of Environmentally Important Processes: Reduction Potentials. *J. Chem. Educ.* **2004**, *81*, 596–604.
- (17) Kelly, C. P.; Cramer, C. J.; Truhlar, D. G. Aqueous Solvation Free Energies of Ions and Ion–Water Clusters Based on an Accurate Value for the Absolute Aqueous Solvation Free Energy of the Proton. *J. Phys. Chem. B* **2006**, *110*, 16066–16081.
- (18) Winter, B.; Faubel, M. Photoemission from Liquid Aqueous Solutions. *Chem. Rev.* **2006**, *106*, 1176–1211.
- (19) Moens, J.; Seidel, R.; Geerlings, P.; Faubel, M.; Winter, B.; Blumberger, J. Energy Levels and Redox Properties of Aqueous $\text{Mn}^{2+/3+}$ from Photoemission Spectroscopy and Density Functional Molecular Dynamics Simulation. *J. Phys. Chem. B* **2010**, *114*, 9173–9182.
- (20) Seidel, R.; Thurmer, S.; Moens, J.; Geerlings, P.; Blumberger, J.; Winter, B. Valence Photoemission Spectra of Aqueous $\text{Fe}^{2+/3+}$ and $[\text{Fe}(\text{CN})_6]^{4-/3-}$ and Their Interpretation by DFT Calculations. *J. Phys. Chem. B* **2011**, *115*, 11671–11677.

- (21) Seidel, R.; Thurmer, S.; Winter, B. Photoelectron Spectroscopy Meets Aqueous Solution: Studies from a Vacuum Liquid Microjet. *J. Phys. Chem. Lett.* **2011**, *2*, 633–641.
- (22) Seidel, R.; Faubel, M.; Winter, B.; Blumberger, J. Single-Ion Reorganization Free Energy of Aqueous $\text{Ru}(\text{bpy})_3^{2+/3+}$ and $\text{Ru}(\text{H}_2\text{O})_6^{2+/3+}$ from Photoemission Spectroscopy and Density Functional Molecular Dynamics Simulation. *J. Am. Chem. Soc.* **2009**, *131*, 16127–16137.
- (23) Marcus, R. A. On the Theory of Electron Transfer Reactions. VI. Unified Treatment for Homogeneous and Electrode Reactions. *J. Chem. Phys.* **1965**, *43*, 679–701.
- (24) Miertuš, S.; Scrocco, E.; Tomasi, J. Electrostatic Interaction of a Solute with a Continuum. A Direct Utilization of Ab Initio Molecular Potentials for the Prediction of Solvent Effects. *Chem. Phys.* **1981**, *55*, 117–129.
- (25) Cramer, C. J.; Truhlar, D. G. Implicit Solvation Models: Equilibria, Structure, Spectra, and Dynamics. *Chem. Rev.* **1999**, *99*, 2161–2200.
- (26) Tomasi, J.; Mennucci, B.; Cammi, R. Quantum Mechanical Continuum Solvation Models. *Chem. Rev.* **2005**, *105*, 2999–3093.
- (27) Barth, S.; Oncak, M.; Ulrich, V.; Mucke, M.; Lischke, T.; Slavicek, P.; Hergenroth, U. Valence Ionization of Water Clusters: From Isolated Molecules to Bulk. *J. Phys. Chem. A* **2009**, *113*, 13519–13527.
- (28) Lange, A. W.; Herbert, J. M. Polarizable Continuum Reaction-Field Solvation Models Affording Smooth Potential Energy Surfaces. *J. Phys. Chem. Lett.* **2010**, *1*, 556–561.
- (29) Ghosh, D.; Roy, A.; Seidel, R.; Winter, B.; Bradforth, S.; Krylov, A. I. First-Principle Protocol for Calculating Ionization Energies and Redox Potentials of Solvated Molecules and Ions: Theory and Application to Aqueous Phenol and Phenolate. *J. Phys. Chem. B* **2012**, *116*, 7269–7280.
- (30) Winter, B. Liquid Microjet for Photoelectron Spectroscopy. *Nucl. Instrum. Methods Phys. Res., Sect. A* **2009**, *601*, 139–150.
- (31) Ottosson, N.; Faubel, M.; Bradforth, S. E.; Jungwirth, P.; Winter, B. Photoelectron Spectroscopy of Liquid Water and Aqueous Solution: Electron Effective Attenuation Lengths and Emission-Angle Anisotropy. *J. Electron Spectrosc. Relat. Phenom.* **2010**, *177*, 60–70.
- (32) Frisch, M. J.; Trucks, G. W.; Schlegel, H. B.; Scuseria, G. E.; Robb, M. A.; Cheeseman, J. R.; Scalmani, G.; Barone, V.; Mennucci, B.; Petersson, G. A., et al. *Gaussian09*; Gaussian, Inc.: Wallingford, CT, 2009.
- (33) Persson, I. Hydrated Metal Ions in Aqueous Solution: How Regular Are Their Structures? *Pure Appl. Chem.* **2010**, *82*, 1901–1917.
- (34) Ohtaki, H.; Radnai, T. Structure and Dynamics of Hydrated Ions. *Chem. Rev.* **1993**, *93*, 1157–1204.
- (35) Richens, D. T. *The Chemistry of Aqua Ions*; John Wiley & Sons: New York, 1997.
- (36) Bock, C. W.; Markham, G. D.; Katz, A. K.; Glusker, J. P. The Arrangement of First- and Second-Shell Water Molecules Around Metal Ions: Effects of Charge and Size. *Theor. Chem. Acc.* **2006**, *115*, 100–112.
- (37) Jaque, P.; Marenich, A. V.; Cramer, C. J.; Truhlar, D. G. Computational Electrochemistry: The Aqueous $\text{Ru}^{3+}|\text{Ru}^{2+}$ Reduction Potential. *J. Phys. Chem. C* **2007**, *111*, 5783–5799.
- (38) Markham, G. D.; Glusker, J. P.; Bock, C. W. The Arrangement of First- and Second-Sphere Water Molecules in Divalent Magnesium Complexes: Results from Molecular Orbital and Density Functional Theory and from Structural Crystallography. *J. Phys. Chem. B* **2002**, *106*, 5118–5134.
- (39) Moens, J.; Roos, G.; Jaque, P.; De Proft, F.; Geerlings, P. Can Electrophilicity Act as a Measure of the Redox Potential of First-Row Transition Metal Ions? *Chem.—Eur. J.* **2007**, *13*, 9331–9343.
- (40) Moens, J.; Jaque, P.; De Proft, F.; Geerlings, P. The Study of Redox Reactions on the Basis of Conceptual DFT Principles: EEM and Vertical Quantities. *J. Phys. Chem. A* **2008**, *112*, 6023–6031.
- (41) Uudsemaa, M.; Tamm, T. Calculations of Hydrated Titanium Ion Complexes: Structure and Influence of the First Two Coordination Spheres. *Chem. Phys. Lett.* **2001**, *342*, 667–672.
- (42) Uudsemaa, M.; Tamm, T. Density-Functional Theory Calculations of Aqueous Redox Potentials of Fourth-Period Transition Metals. *J. Phys. Chem. A* **2003**, *107*, 9997–10003.
- (43) Becke, A. D. Density-Functional Exchange-Energy Approximation with Correct Asymptotic Behavior. *Phys. Rev. A* **1988**, *38*, 3098–3100.
- (44) Lee, C. T.; Yang, W. T.; Parr, R. G. Development of the Colle–Salvetti Correlation-Energy Formula into a Functional of the Electron Density. *Phys. Rev. B* **1988**, *37*, 785–789.
- (45) Perdew, J. P.; Burke, K.; Ernzerhof, M. Generalized Gradient Approximation Made Simple. *Phys. Rev. Lett.* **1996**, *77*, 3865–3868.
- (46) Krieger, J. B.; Chen, J.; Iafrate, G. J.; Savin, A. In *Electron Correlations and Materials Properties*; Gonis, A., Kioussis, N., Ciftan, M., Eds.; Plenum Publishers: New York, 1999; p 463.
- (47) Tao, J. M.; Perdew, J. P.; Staroverov, V. N.; Scuseria, G. E., Climbing the Density Functional Ladder: Nonempirical Meta-Generalized Gradient Approximation Designed for Molecules and Solids. *Phys. Rev. Lett.* **2003**, *91*.
- (48) Zhao, Y.; Truhlar, D. G., A New Local Density Functional for Main-Group Thermochemistry, Transition Metal Bonding, Thermochemical Kinetics, and Noncovalent Interactions. *J. Chem. Phys.* **2006**, *125*.
- (49) Stephens, P. J.; Devlin, F. J.; Chabalowski, C. F.; Frisch, M. J. Ab Initio Calculation of Vibrational Absorption and Circular Dichroism Spectra Using Density Functional Force Fields. *J. Phys. Chem.* **1994**, *98*, 11623–11627.
- (50) Adamo, C.; Cossi, M.; Barone, V. An Accurate Density Functional Method for the Study of Magnetic Properties: The PBE0 Model. *J. Mol. Struct.: THEOCHEM* **1999**, *493*, 145–157.
- (51) Ernzerhof, M.; Scuseria, G. E. Assessment of the Perdew–Burke–Ernzerhof Exchange–Correlation Functional. *J. Chem. Phys.* **1999**, *110*, 5029–5036.
- (52) Zhao, Y.; Schultz, N. E.; Truhlar, D. G., Exchange–Correlation Functional with Broad Accuracy for Metallic and Nonmetallic Compounds, Kinetics, and Noncovalent Interactions. *J. Chem. Phys.* **2005**, *123*.
- (53) Zhao, Y.; Schultz, N. E.; Truhlar, D. G. Design of Density Functionals by Combining the Method of Constraint Satisfaction with Parametrization for Thermochemistry, Thermochemical Kinetics, and Noncovalent Interactions. *J. Chem. Theory Comput.* **2006**, *2*, 364–382.
- (54) Zhao, Y.; Truhlar, D. G. The M06 Suite of Density Functionals for Main Group Thermochemistry, Thermochemical Kinetics, Noncovalent Interactions, Excited States, and Transition Elements: Two New Functionals and Systematic Testing of Four M06-Class Functionals and 12 Other Functionals. *Theor. Chem. Acc.* **2008**, *120*, 215–241.
- (55) Hariharan, P. C.; Pople, J. A. The Influence of Polarization Functions on Molecular Orbital Hydrogenation Energies. *Theor. Chim. Acta* **1973**, *28*, 213–222.
- (56) Dolg, M.; Wedig, U.; Stoll, H.; Preuss, H. Energy-Adjusted Ab Initio Pseudopotentials for the First Row Transition Elements. *J. Chem. Phys.* **1987**, *86*, 866–872.
- (57) Dunning, T. H. Gaussian Basis Sets for Use in Correlated Molecular Calculations. I. The Atoms Boron through Neon and Hydrogen. *J. Chem. Phys.* **1989**, *90*, 1007–1023.
- (58) Balabanov, N. B.; Peterson, K. A. Systematically Convergent Basis Sets for Transition Metals. I. All-Electron Correlation Consistent Basis Sets for the 3d Elements Sc–Zn. *J. Chem. Phys.* **2005**, *123*, 64107.
- (59) Jansen, G.; Hess, B. A. Revision of the Douglas–Kroll Transformation. *Phys. Rev. A* **1989**, *39*, 6016–6017.
- (60) Douglas, M.; Kroll, N. M. Quantum Electrodynamical Corrections to the Fine Structure of Helium. *Ann. Phys.* **1974**, *82*, 89–155.
- (61) Srnec, M.; Chalupský, J.; Fojta, M.; Zendlová, L.; Havran, L.; Hocek, M.; Kývala, M.; Rulíšek, L. Effect of Spin–Orbit Coupling on

Reduction Potentials of Octahedral Ruthenium(II/III) and Osmium(II/III) Complexes. *J. Am. Chem. Soc.* **2008**, *130*, 10947–10954.

(62) Tsushima, S.; Wahlgren, U.; Grenthe, I. Quantum Chemical Calculations of Reduction Potentials of $\text{AnO}_2^{2+}/\text{AnO}_2^+$ ($\text{An} = \text{U, Np, Pu, Am}$) and $\text{Fe}^{3+}/\text{Fe}^{2+}$ Couples. *J. Phys. Chem. A* **2006**, *110*, 9175–9182.

(63) Tomasi, J.; Mennucci, B.; Cances, E. The IEF Version of the PCM Solvation Method: An Overview of a New Method Addressed to Study Molecular Solutes at the QM Ab Initio Level. *J. Mol. Struct.: THEOCHEM* **1999**, *464*, 211–226.

(64) Møller, C.; Plesset, M. S. Note on an Approximation Treatment for Many-Electron Systems. *Phys. Rev.* **1934**, *46*, 618–622.

(65) Noga, J.; Bartlett, R. J. The Full CCSDT Model for Molecular Electronic Structure. *J. Chem. Phys.* **1987**, *86*, 7041–7050.

(66) Rehr, J. J.; Albers, R. C. Theoretical Approaches to X-ray Absorption Fine Structure. *Rev. Mod. Phys.* **2000**, *72*, 621–654.

(67) Allen, F. H. The Cambridge Structural Database: A Quarter of a Million Crystal Structures and Rising. *Acta Crystallogr., Sect. B: Struct. Sci.* **2002**, *58*, 380–388.

(68) Beattie, J. K.; Best, S. P.; Skelton, B. W.; White, A. H. Structural Studies on the Caesium Alums, $\text{CsM}[\text{SO}_4]_2 \cdot 12\text{H}_2\text{O}$. *J. Chem. Soc., Dalton Trans.* **1981**, 2105–2111.

(69) Kristiansson, O.; Persson, I.; Bobicz, D.; Xu, D. W. A Structural Study of the Hydrated and the Dimethylsulfoxide, $\text{N,N}'$ -Dimethylpropyleneurea, Acetonitrile, Pyridine and N,N -Dimethylthioformamide Solvated Nickel(II) Ion in Solution and Solid State. *Inorg. Chim. Acta* **2003**, *344*, 15–27.

(70) Lindqvist-Reis, P.; Munoz-Paez, A.; Diaz-Moreno, S.; Pattanaik, S.; Persson, I.; Sandstrom, M. The Structure of the Hydrated Gallium(III), Indium(III), and Chromium(III) Ions in Aqueous Solution. A Large Angle X-ray Scattering and EXAFS Study. *Inorg. Chem.* **1998**, *37*, 6675–6683.

(71) Tachikawa, H.; Ichikawa, T.; Yoshida, H. Hydration Structure of Titanium(III) Ion – ESR and Electron Spin-Echo Study. *J. Am. Chem. Soc.* **1990**, *112*, 977–982.

(72) Aquino, M. A. S.; Clegg, W.; Liu, Q. T.; Sykes, A. G. Hexaqua-titanium(III) Tris(p-toluenesulfonate) Trihydrate. *Acta Crystallogr., Sect. C: Cryst. Struct. Commun.* **1995**, *51*, S60–S62.

(73) Akesson, R.; Pettersson, L. G. M.; Sandstrom, M.; Wahlgren, U. Theoretical Calculations of the Jahn–Teller Effect in the Hexahydrated Copper(II), Chromium(II), and Manganese(III) Ions, $[\text{Cu}(\text{H}_2\text{O})_6]^{2+}$, $[\text{Cr}(\text{H}_2\text{O})_6]^{2+}$, and $[\text{Mn}(\text{H}_2\text{O})_6]^{3+}$, and Comparisons with the Hexahydrated Copper(I), Chromium(III), and Manganese(II) Clusters. *J. Phys. Chem.* **1992**, *96*, 150–156.

(74) Persson, I.; Persson, P.; Sandstrom, M.; Ullstrom, A. S. Structure of Jahn–Teller Distorted Solvated Copper(II) Ions in Solution, and in Solids with Apparently Regular Octahedral Coordination Geometry. *J. Chem. Soc., Dalton Trans.* **2002**, 1256–1265.

(75) Blumberger, J. $\text{Cu}_{\text{aq}}^+/\text{Cu}_{\text{aq}}^{2+}$ Redox Reaction Exhibits Strong Nonlinear Solvent Response Due to Change in Coordination Number. *J. Am. Chem. Soc.* **2008**, *130*, 16065–16068.

(76) Frank, P.; Benfatto, M.; Szilagyi, R. K.; D'Angelo, P.; Della Longa, S.; Hodgson, K. O. The Solution Structure of $[\text{Cu}(\text{aq})]^{2+}$ and Its Implications for Rack-Induced Bonding in Blue Copper Protein Active. *Inorg. Chem.* **2005**, *44*, 1922–1933.

(77) Blumberger, J.; Bernasconi, L.; Tavernelli, I.; Vuilleumier, R.; Sprik, M. Electronic Structure and Solvation of Copper and Silver Ions: A Theoretical Picture of a Model Aqueous Redox Reaction. *J. Am. Chem. Soc.* **2004**, *126*, 3928–3938.

(78) Alajlouni, A. M.; Espenson, J. H.; Bakac, A. Reaction of Hydrogen Peroxide with the Oxochromium(IV) Ion by Hydride Transfer. *Inorg. Chem.* **1993**, *32*, 3162–3165.

(79) *Standard Potentials in Aqueous Solution*; Bard, A. J., Parsons, R., Jordan, J., Eds.; Marcel Dekker: New York, 1985.

(80) Bratsch, S. G. Standard Electrode-Potentials and Temperature Coefficients in Water at 298.15-K. *J. Phys. Chem. Ref. Data* **1989**, *18*, 1–21.

(81) Lide, D. R. *CRC Handbook of Chemistry and Physics*; CRC Press: Boca Raton, FL, 2002.

(82) Winter, B.; Weber, R.; Hertel, I. V.; Faubel, M.; Jungwirth, P.; Brown, E. C.; Bradforth, S. E. Electron Binding Energies of Aqueous Alkali and Halide Ions: EUV Photoelectron Spectroscopy of Liquid Solutions and Combined Ab Initio and Molecular Dynamics Calculations. *J. Am. Chem. Soc.* **2005**, *127*, 7203–7214.

(83) Winter, B.; Weber, R.; Widdra, W.; Dittmar, M.; Faubel, M.; Hertel, I. V. Full Valence Band Photoemission from Liquid Water Using EUV Synchrotron Radiation. *J. Phys. Chem. A* **2004**, *108*, 2625–2632.

(84) Eastman, D. E.; Freeouf, J. L. Photoemission Partial State Densities of Overlapping p and d States for NiO, CoO, FeO, MnO, and Cr_2O_3 . *Phys. Rev. Lett.* **1975**, *34*, 395–398.

(85) Sugano, S.; Tanabe, Y.; Kamimura, H. *Multiplets of Transition-Metal Ions in Crystals*; Academic Press: New York, 1970.

(86) Huheey, J. E.; Keiter, E. A.; Keiter, R. L. *Inorganic Chemistry: Principles of Structures and Reactivity*; HarperCollins College Publishers: New York, 1993.

(87) Schultz, N. E.; Zhao, Y.; Truhlar, D. G. Density Functionals for Inorganometallic and Organometallic Chemistry. *J. Phys. Chem. A* **2005**, *109*, 11127–11143.

(88) Schultz, N. E.; Zhao, Y.; Truhlar, D. G. Databases for Transition Element Bonding: Metal–Metal Bond Energies and Bond Lengths and Their Use to Test Hybrid, Hybrid Meta, and Meta Density Functionals and Generalized Gradient Approximations. *J. Phys. Chem. A* **2005**, *109*, 4388–4403.

(89) Reed, A. E.; Curtiss, L. A.; Weinhold, F. Intermolecular Interactions from a Natural Bond Orbital, Donor–Acceptor Viewpoint. *Chem. Rev.* **1988**, *88*, 899–926.

(90) Trasatti, S. The Absolute Electrode Potential – An Explanatory Note (Recommendations 1986). *Pure Appl. Chem.* **1986**, *58*, 955–966.

(91) Blumberger, J.; Lamoureux, G. Reorganization Free Energies and Quantum Corrections for a Model Electron Self-Exchange Reaction: Comparison of Polarizable and Non-Polarizable Solvent Models. *Mol. Phys.* **2008**, *106*, 1597–1611.

(92) Oberhofer, H.; Blumberger, J. Insight into the Mechanism of the Ru^{2+} – Ru^{3+} Electron Self-Exchange Reaction from Quantitative Rate Calculations. *Angew. Chem., Int. Ed.* **2010**, *49*, 3631–3634.

(93) Tateyama, Y.; Blumberger, J.; Ohno, T.; Sprik, M. Free Energy Calculation of Water Addition Coupled to Reduction of Aqueous RuO_4 . *J. Chem. Phys.* **2007**, *126*, 204506.